ICLASS 2018, 14th Triennial International Conference on Liquid Atomization and Spray Systems, Chicago, IL, USA, July 22-26, 2018

DNS of Multiple Bubble Growth and Droplet Formation in Superheated Liquids

D. Loureiro[1]*, J. Reutzsch[2], D. Dietzel[1],A. Kronenburg[1], B. Weigand[2], K. Vogiatzaki [3]
[1]Institute for Combustion Technology, University of Stuttgart, Germany
[2]Institute of Aerospace Thermodynamics, University of Stuttgart, Germany
[3]Advanced Engineering Centre, University of Brighton, UK

Abstract

Flash boiling can occur in rocket thrusters used for orbital manoeuvring of spacecraft as the cryogenic propellants are injected into the vacuum of space. For reliable ignition, a precise control of the atomization process is required as atomization and mixing of fuel and oxidizer are crucial for the subsequent combustion process. This work focuses on the microscopic process leading to the primary break-up of a liquid oxygen jet, caused by homogeneous nucleation and growth of vapour bubbles in superheated liquid. Although large levels of superheat can be achieved, sub-critical injection conditions ensure distinct gas and liquid phases with a large density ratio. Direct numerical simulations (DNS) are performed using the multiphase solver FS3D. The code solves the incompressible Navier-Stokes equations using the Volume of Fluid (VOF) method and PLIC reconstruction for the phase interface treatment. The interfaces are tracked as multiple bubbles grow, deform and coalesce, leading to the formation of a spray. The evaporation rate at the interface and approximate vapour properties are based on pre-computed solutions resolving the thermal boundary layer surrounding isolated bubbles, while liquid inertia and surface tension effects are expected to play a major role in the final spray characteristics which can only be captured by DNS. Simulations with regular arrays of bubbles demonstrate how the initial bubble spacing and thermodynamic conditions lead to distinct spray characteristics and droplet size distributions.

Introduction

Small rocket thrusters that are used for orbital manoeuvring as well as some re-ignitable upper-stage rocket engines typically rely on hypergolic propellants such as hydrazine and its derivatives. These can be highly toxic and corrosive causing safety and environmental concerns, as well as ground handling costs. This has motivated research [1, 2] towards replacing these systems with cryogenic bi-propellant alternatives. The most likely choices would be liquid hydrogen, methane or kerosene in combination with liquid oxygen, i.e. the same fuel-oxidizer combinations as used for the primary propulsion system of the spacecraft or the booster stage. The atomization and mixing process of fuel and oxidizer in the combustion chamber is crucial, as it will affect the reliability of the ignition and the efficiency of the subsequent combustion process. Because these thrusters operate at very high altitude or in the vacuum of space, the extremely low pressure conditions lead to the phenomenon of flash boiling, or flashing, which is the main focus of this work.

Flashing occurs when a liquid experiences a rapid drop in pressure to a value below its saturation condition. In this meta-stable superheated state, microscopic vapour bubbles spontaneously nucleate within the continuous liquid phase (homogeneous nucleation). This is followed by rapid expansion that leads to the jet disintegration and extremely fast evaporation. Fast jet break-up is generally beneficial for the atomization process as it leads to finer droplets and large jet spreading angles.

Bubble growth can be characterized by several stages. First, stable nuclei form with a critical radius given by $R_{\mathrm{crit}} = 2\sigma/\left(p_{\mathrm{sat}}(T_\infty) - p_\infty\right)$ where σ is the surface tension coefficient and the subscripts, sat, and, ∞, denote saturation and injection conditions. For small disturbances, the bubble grows at an exponential rate as the surface tension drops and the vapour pressure is balanced by the inertia of the surrounding liquid only. This is the *inertia controlled* stage of growth. During this process, the interface temperature T_Γ decreases due to the latent heat of evaporation and a thermal boundary layer develops around the bubble. The vapour pressure decreases and the evaporation rate becomes limited by the supply of heat to the interface through conduction. After reaching a peak, the growth rate continuously decelerates as the liquid cools, and this stage is labelled *thermal diffusion controlled.*

An isolated bubble would grow until all the liquid has evaporated or cooled below saturation temperature. However, in a real flashing jet a large number of bubbles will nucleate simultaneously and coalesce, leading to the formation of the spray. The nucleation rate J defines the number of bubbles nucleating per unit volume and time

*Corresponding author: daniel.dias-loureiro@itv.uni-stuttgart.de

and can be estimated for homogeneous nucleation, e.g. [3, 4], as

$$J \propto \exp\left(\frac{-\Delta G}{kT_\ell}\right), \tag{1}$$

where ΔG is the Gibbs energy and k is the Boltzmann constant. Due to the exponential function, this model is highly sensitive to the correct value of ΔG and the proportionality factor. Despite this uncertainty and possible additional nucleation triggered by cavitation and heterogeneous nucleation inside the nozzle, many experimental works [5, 6, 7] continue to correlate the spray characteristics with this type of model. This leads to poor predictability of the spray characteristics through J only. Furthermore, the accuracy of experimental methods is often limited by the lack of knowledge about the distribution of droplet sizes and the assumption of spherical droplet shapes.

Conventional numerical studies on flashing jets such as [8, 9] employ a two phase mixture model. The nucleation of individual bubbles is not resolved and relies on a mass-transfer rate derived from kinetic theory of gases or on relaxation models for vapour generation which require calibration. Other approaches using Eulerian-Lagrangian methods (cf. [10, 11]) rely on empirical models for the initial droplet size distribution and various additional assumptions on droplet shapes and relative velocities. Models for break-up due to bubble growth and aerodynamic forces that are based on linear stability analysis have also been employed [12]. Generally, all these approaches lack information about the actual break-up process at the microscopic scale, one of them being the interaction of multiple bubbles.

In this work a framework is presented to perform numerical calculations of the primary break-up process resulting from bubble nucleation and growth, that are typically neither covered by conventional fluid dynamics simulations nor directly observed in experimental methods. We conduct direct numerical simulations (DNS) for free surface multiphase flows where the term DNS refers to the full resolution of the interfaces of the individual bubbles and of all the spatial turbulent scales that are relevant for the break-up process. The set-up is representative of the conditions that can be found inside the injector or within large liquid structures that are injected into the combustion chamber. The growth, deformation and coalescence of multiple interacting bubbles is simulated. This includes the formation of ligaments and lamellae, their break-up due to capillary forces and evaporation of the superheated liquid. By resolving such structures, different break-up regimes can be identified and compared with known models and experiments for primary and secondary jet atomization such as the classical Rayleigh instability analysis [13] , droplet collisions [14] and aerodynamic droplet break-up scenarios [15]. With this insight, the spray characteristics can be better predicted, and estimates of surface area to volume ratios and droplet velocity can be provided. These can then be used to develop new sub-grid-scale models for large scale numerical simulations and for the validation of existing approximate models.

The work presented here focuses on the break-up behaviour of a flashing liquid oxygen (LOx) jet. The range of conditions is based on corresponding experiments at the Institute of Space Propulsion at DLR in Lampoldshausen [5]. Typical temperatures of the injected LOx are in the ranges of $T_\infty \in [80, 120]$ K and typical chamber pressures are $p_\infty \in \left[10^3, 10^5\right]$ Pa.

Numerical tools and methods

Due to the different resolution requirements and time scales involved the thermodynamics of bubble growth are decoupled from the fluid-mechanical processes of jet break-up. For a given thermodynamic condition defined by p_∞ and T_∞, we first determine the growth rate and fluid properties of a single bubble as a function of bubble size. These computations include well resolved heat exchanges at the interface and variable fluid properties. Then, these results can be used as an approximate model for the evaporation mass fluxes in free-surface multiphase DNS simulations. The latter include the growth of multiple interacting bubbles with capillary effects and provide statistics for the formation of a spray and the resulting droplet size distribution.

Spherical bubble growth

The growth dynamics of an isolated spherical bubble can be described by the Rayleigh-Plesset equation

$$R\ddot{R} + \frac{3}{2}\dot{R}^2 = \frac{1}{\rho_\ell}\left(p_v - p_\infty - \frac{2\sigma}{R} - \frac{4\mu_\ell}{R}\dot{R}\right), \tag{2}$$

where the driving force for growth is the internal vapour pressure p_v. The method of Lee and Merte [16] is used to integrate this equation in time. Assuming saturation conditions and a uniform temperature distribution in the vapour phase, the vapour pressure is $p_v = p_{\mathrm{sat}}(T_\Gamma)$, and can be determined from the interface temperature T_Γ which is obtained by coupling the Rayleigh-Plesset equation with the energy conservation equation. The latter

is solved using a finite difference method in spherical coordinates, fully resolving the thermal boundary layer surrounding the bubble. The boundary condition at the interface ensures that the heat flux matches the latent heat of evaporation. The saturation pressure and all relevant fluid properties including vapour density and surface tension coefficient are obtained as functions of T_Γ using the Equation-of-State library CoolProp [17]. This method is able to capture the continuous transition between the equilibrium state for the critical radius, the inertia controlled stage and the thermal diffusion controlled stage as the bubble radius grows by several orders of magnitude. As the 1-D computations are relatively inexpensive, a database for the range of ambient conditions (p_∞, T_∞) of interest is built, such that the bubble growth rate $\dot{R}$ and the interface temperature T_Γ can be read from the table as a function of time or bubble radius.

To compare the general growth behaviour between different thermodynamic conditions, we normalize the bubble radius using the critical nucleation radius $R^* = R/R_{\mathrm{crit}}$. Results for selected temperatures at the high and low ends of the pressure range are presented in Fig. 1. Figure 1(a) shows that the growth rate peaks when the bubbles size has reached about 10 times its critical radius. Subsequently, the decrease of the growth rate is relatively slow. The same is observed for the interface temperature (Fig. 1(b)) which determines the vapour properties and surface tension coefficient (Fig. 1(c)). These observations serve as basis for the modelling of the evaporation mass flux, $\dot{m}''$, that requires closure in the DNS simulations, and this is discussed in more detail in the following section.

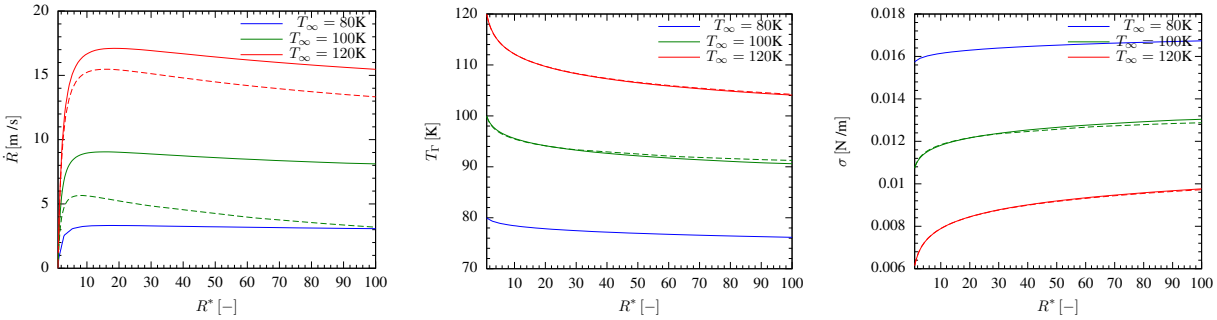

(a) Growth rate $\dot{R}$ (b) Interface temperature T_Γ (c) Surface tension σ

Figure 1. Results from the 1-D solution as function of relative bubble size $R^* = R/R_{\mathrm{crit}}$ for the range of liquid temperatures T_∞ (80 K to 120 K) and pressures $p_\infty = 10^3$ Pa (solid lines) and $p_\infty = 10^5$ Pa (dashed lines).

Multiphase DNS of multiple bubble growth

We use the code Free Surface 3D (FS3D) [18] for the multiphase DNS simulations. The incompressible Navier-Stokes equations are solved and the phase tracking is realized by a Volume-of-Fluid method (VoF). In the VoF method, an additional transport equation is used to advect the variable f which represents the volume fraction of the liquid. It is written as

$$\frac{\partial f}{\partial t} + \nabla \cdot (f \mathbf{u}_\Gamma) = \frac{-\dot{m}'''}{\rho_\ell}, \tag{3}$$

where $\mathbf{u}_\Gamma$ is the interface velocity and $\dot{m}'''$ accounts for the evaporating liquid mass per unit volume. The interface area density a_Γ ($\mathrm{m}^2/\mathrm{m}^3$) and the interface normal $\hat{\mathbf{n}}$ are obtained by reconstructing the interface geometry from the f field with the piecewise linear interface calculation (PLIC) algorithm. The fluid density, viscosity and other properties can be determined as a mass-averaged continuous field based on the VoF, e.g. $\rho = \rho_\ell f + \rho_v (1 - f)$, and then be used to solve the Navier-Stokes equations for a continuous velocity and pressure field, viz.

$$\frac{\partial}{\partial t}(\rho \mathbf{u}) + \nabla \cdot [\rho \mathbf{u}\mathbf{u}] = \nabla \cdot \mu \left[\nabla \mathbf{u} + \nabla (\mathbf{u})^{\mathsf{T}}\right] - \nabla p + f_\sigma. \tag{4}$$

The surface tension force is introduced as a volumetric force, f_σ, acting only on the cells containing the interface. The continuum surface stress model (CSS) [19] is used since it is compatible with interface collisions and break-up upon bubble coalescence and droplet merging. The pressure field is obtained using an efficient multigrid solver for the Poisson equation. Due to the mass transfer with a high density ratio between the liquid and vapour phases, the divergence of the velocity field, $\nabla \cdot \mathbf{u}$, is included to introduce the necessary jump condition in the continuity equation that accounts for the evaporation rate, $\dot{m}'''$, as detailed in [20].

Defining the evaporation rate as $\dot{m}''' = a_\Gamma \dot{m}''$, a closure equation is required for the mass flux across the interface $\dot{m}''$. In the present approach, an approximate method is used, relying on the growth rates obtained from the 1-D solutions as presented in Fig. 1. The growth rate of a spherical bubble, $\dot{R}$, is equivalent to the interface velocity relative to the bubble's centre and can be defined as

$$\dot{R} \equiv \mathbf{u}_\Gamma - \mathbf{u}_{\text{centre}} = -\dot{m}''/\rho_v \cdot \hat{\mathbf{n}}. \tag{5}$$

Using the definition for the curvature of a sphere, $\kappa = 2/R$, we map the 1-D solution for the growth rate as function of radius $\dot{R}(R)$ to a function of curvature $\dot{R}(\kappa)$. Together with Eq. (5), we model $\dot{m}''$ as

$$\dot{m}'' = -\rho_v \dot{R}(\kappa), \tag{6}$$

where $\kappa = -\nabla \cdot (\nabla f/|\nabla f|)$ is positive for a bubble and negative for droplet shapes.

The maximum curvature corresponds to the critical radius. As the bubbles grow, κ asymptotes towards zero until they start to influence each other and deform. At this point, the curvature may quickly change to negative values as break-up occurs and droplets form. Although evaporation of ligaments and droplets continues, the evaporative mass flux can no longer be correlated with curvature. Assuming a negligible effect of the surface tension on large bubbles, the vapour pressure (and interface temperature) of the coalesced bubbles is similar to the pressure just before merging. Thus, defining R_f as the maximum radius of the bubbles before coalescence, the growth rate $\dot{R}(R_f)$ can be used as a good approximation for $\dot{m}''$ at point of liquid jet break-up and beyond. The evaporation rate model is therefore closed by introducing the appropriate limits to Eq. (6), i.e.

$$\dot{m}'' = \begin{cases} -\rho_v \dot{R}(2/R_f) & \text{if } \kappa < 2/R_f \\ -\rho_v \dot{R}(\kappa) & \text{if } 2/R_f \leq \kappa \leq 2/R_{\text{crit}} \\ 0 & \text{if } \kappa > 2/R_{\text{crit}} \end{cases}. \tag{7}$$

A lookup table is built for each p_∞ and T_∞ condition. One advantage of this tabulation approach using the 1D Rayleigh-Plesset solution is that it introduces the initial acceleration transient of the bubble growth despite the use of an incompressible DNS solver. The suggested closure provides a good approximation during the early stages of the growth process while bubbles remain spherical. But even for larger bubbles, that may deform due to reduced surface tension forces and due to bubble-bubble interactions, the -then constant- growth rate provides a sufficiently adequate model as $\dot{m}''$ is nearly constant during the diffusion controlled stage (cf. Fig. 1).

The main limitations are (1) that the final evaporation rate of the resulting liquid structures relies on the estimation of R_f, implying a regular bubble distribution and (2) that it does not account for further variation of the evaporation rate due to any changes in vapour pressure for the coalesced bubble. The latter may affect results when merging occurs during the inertia dominated stage of growth or when cooling reduces the temperature of the droplets after break-up. Thus, this implementation is adequate to develop the correct fluid velocity fields leading to break-up but may require improved closures for the modelling of subsequent evaporation of droplets and ligaments.

Set-up method

The simulation set-up represents a small volume of continuous liquid inside the injector nozzle or a large droplet, that is sufficiently far from any walls as depicted in Fig. 2. The reference temperature and pressure conditions of the DNS, T_∞ and p_∞ correspond to local conditions that could be found in the relevant jet section. Assuming negligible liquid cooling upstream, T_∞ is the reservoir temperature. Although p_∞ could take any value between p_{chamber} and $p_{\text{sat}}(T_\ell)$, it is expected that the influence of the pressure on the fluid properties is small and only the lowest pressure of the range $p_\infty = 1000\,\text{Pa}$ is simulated. Table 1 shows the temperatures simulated and the corresponding level of superheat $\Delta T = T_{\text{sat}}(p_\infty) - T_\infty$, pressure ratio $R_p = p_{\text{sat}}(T_\infty)/p_\infty$, and critical radius R_{crit}.

Table 1. Superheat and critical radius for Oxygen at $p_\infty = 1000\,\text{Pa}$

T_∞	80 K	100 K	120 K
ΔT	18.71	38.71	58.71
R_p	30.12	254	1022
R_{crit}(m)	1.081×10^{-6}	8.487×10^{-8}	1.202×10^{-8}

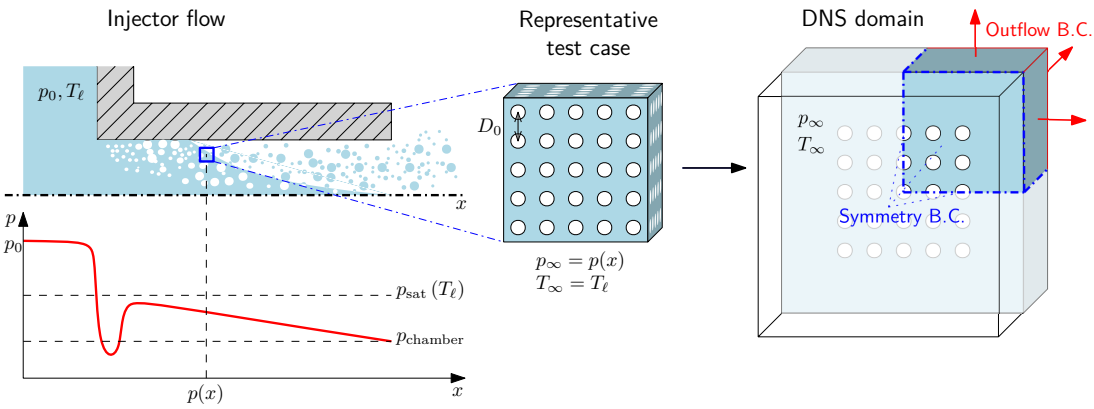

Figure 2. Schematic of flashing flow in the injector (adapted from [21]) and computational domain.

The thermodynamic conditions are given by the corresponding experiments at DLR, but the average bubble radius at which bubble interactions and interface deformations become relevant is treated as a free parameter. The size of the merging bubbles and the initial bubble spacing or bubble number density are directly correlated. As the modelling of the nucleation rate is subject to high uncertainty (see above) we provide here parameter studies for different nucleation rates (bubble distances) and will validate assumptions on nucleation rates and resulting droplets size and velocity distributions by comparison with forthcoming measurements from DLR in future work. Assuming an equidistant bubble distribution, we define R_f as the average radius at which spherical bubbles are expected to touch and start to merge. With $R_f^* = R_f/R_{\text{crit}}$, R_f^* is the growth factor since nucleation and is used as the second set-up parameter. Simulations were performed for the cases $R_f^* = \{2, 5, 10, 50\}$, which comprises cases of bubbles merging in the inertia, transition and heat diffusion controlled stages of growth.

Using the 1-D solution as a reference, R_f^* determines both the limit for the evaporation rate (Eq. (7)) and the interface temperature T_Γ. With $p_v = p_{\text{sat}}(T_\Gamma)$ and $T_v = T_\Gamma$ the vapour properties ρ_v and μ_v, as well as the surface tension coefficient $\sigma(T_\Gamma)$, are determined from CoolProp [17]. The liquid properties ρ_ℓ and μ_ℓ are directly determined as function of p_∞ and T_∞ and remain constant for the entire simulation.

The dynamics of the break-up process depend not only on the bubble size but also require the correct velocity field and dynamic pressure gradients. The bubbles are therefore initialized with an initial radius $R_i \ll R_f$. Depending on R_f^* and available mesh resolution, R_i is either set to R_{crit} or at least one order of magnitude smaller than R_f as 99.9% of the volumetric bubble expansion will occur for the bubble size interval $R \in [0.1R_f, R_f]$. Setting the correct initial bubble spacing ensures that all bubbles in the domain will merge simultaneously at approximately the expected radius R_f. Considering a regular spacing as shown in Fig. 2, the distance between centres D_0 is determined by conservation of mass in the control volume $(2R_f)^3$ and can be formulated as

$$D_0 = R_f \sqrt[3]{8 - \frac{4\pi}{3}\left(1 - \frac{\rho_v}{\rho_\ell}\right)\left(1 - \frac{R_i^3}{R_f^3}\right)}, \tag{8}$$

where R_i is the initial bubble radius. Equation (8) can also be used to obtain the relation between R_f^* and bubble number density, $n = 1/D_0^3$, with $R_i = R_{\text{crit}}$. This translates to number densities ranging from 1.66×10^{12} (for $T_\infty = 80\,\text{K}$, $R_f^* = 50$) to 1.61×10^{22} bubbles/m^3 (for $T_\infty = 120\,\text{K}$, $R_f^* = 2$). The relevant times for possible bubble nucleation span from 8.6×10^{-9} s to 2.1×10^{-5} s, and estimates for corresponding nucleation rates would be 8.1×10^{16} to 1.9×10^{30} bubbles/m^3 s.

The computational domain makes use of symmetry boundary conditions to reduce computational cost and a large buffer zone in order to completely contain the coalesced bubbles and all the droplets generated. The domain length L is defined as function of the number of bubbles N_{bub}, R_f and a factor of 4 for the buffer zone, resulting in

$$L = 4\sqrt[3]{N_{\text{bub}}}R_f. \tag{9}$$

For the present work, the bubble array is initialized with 2.5 bubbles in each direction, representing a case of $N_{\text{bub}} = 125$. For all the simulated cases a Cartesian mesh of $256^3 \approx 17$ million cells is used, i.e. the diameter of the merging bubbles is resolved by approximately 26 cells independently of R_f^* and the thermodynamic conditions. The computational costs range from 150 to 4000 CPU-hours.

Results and discussion

A series of simulations is performed where the liquid temperature T_∞ and the ratio of final bubble size relative to the critical radius, $R_f^* = R_f/R_{\text{crit}}$, are varied. The sequence in Fig. 3 depicts the phase interface at various time steps for an intermediate case with $T_\infty = 100\,\text{K}$, $R_f^* = 10$.

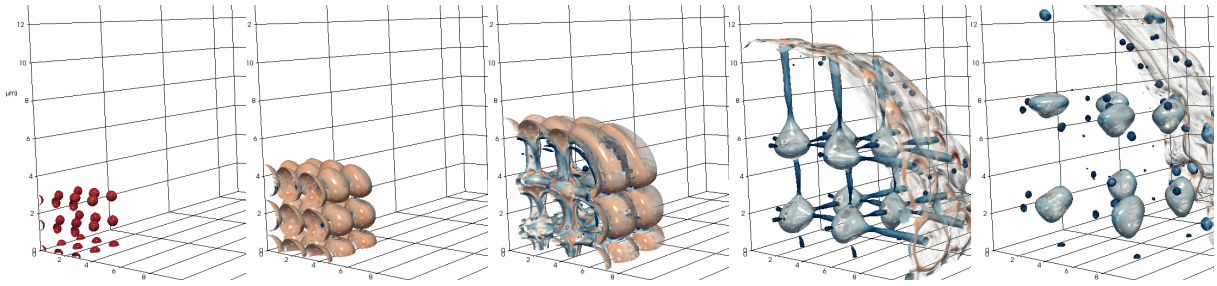

(a) $t = 0.06\,\mu\text{s}$ (b) $t = 0.13\,\mu\text{s}$ (c) $t = 0.20\,\mu\text{s}$ (d) $t = 0.40\,\mu\text{s}$ (e) $t = 0.60\,\mu\text{s}$

Figure 3. Simulation of bubble growth and liquid break-up for the case $p_\infty = 1000\,\text{Pa}$, $T_\infty = 100\,\text{K}$, $R_f^* = 10$, $\text{We}_b = 12.6$. Surfaces correspond to the iso-surface of the volume fraction with $f = 0.5$. The surface is coloured according to curvature as red for bubbles and blue for droplets.

Throughout the range of test cases it is observed that the qualitative characteristics of the break-up process are primarily dictated by R_f^*, and rather independent of T_∞. This observation can be better understood using a classification of the process conditions based on characteristic quantities. Here, we define the Weber, Reynolds and Ohnesorge numbers for the merging bubbles as

$$\text{We}_b = \frac{\rho_\ell \dot{R}_f^2 2R_f}{\sigma}, \qquad \text{Re}_b = \frac{\rho_\ell \dot{R}_f 2R_f}{\mu_\ell} \qquad \text{and} \qquad \text{Oh}_b = \frac{\sqrt{\text{We}_b}}{\text{Re}_b} = \frac{\mu_\ell}{\sqrt{\rho_\ell \sigma 2R_f}}, \tag{10}$$

where the reference quantities are the final bubble diameter, $2R_f = 2R_f^* R_{\text{crit}}$, and the bubble growth rate $\dot{R}_f = \dot{R}(R_f)$, calculated from the 1-D solution for isolated bubbles (cf. Fig. 1) for the corresponding p_∞ and T_∞. The relation between the set-up parameters R_f^* and T_∞ and the characteristic quantities We_b and Oh_b is visualized in Fig. 4.

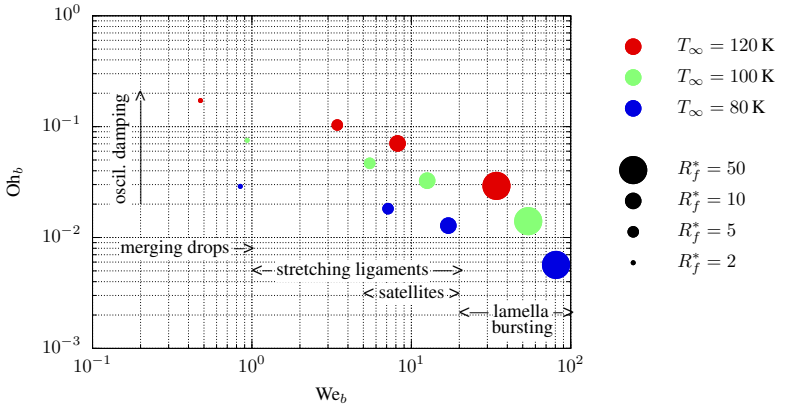

Figure 4. Weber and Ohnesorge number diagram for the 12 test cases. The symbols are coloured according to temperature and the symbol size is proportional to $\log R_f^*$, where $R_f^* = R_f/R_{\text{crit}}$ and R_{crit} is temperature dependent.

For each T_∞ there is an apparent relationship between We_b and R_f^*. However, it should be noted that for a given R_f^*, the range of T_∞ implies a variation of the real radius R_f by two orders of magnitude. There is, however, only a weak dependency of We_b on T_∞, which can be explained by corresponding variations in $\dot{R}$ and σ, that partially negate the variation in R_f. Hence, the Weber number, and thus the type of break-up observed,

is mainly dependent on R_f^* while T_∞ determines a reference length scale through R_{crit}. The Ohnesorge number, Oh_b, depends on both T_∞ and R_f^* and is representative of the viscous damping of capillary driven oscillations. This damping can be observed in simulations where higher Oh_b lead to quicker stabilization of the droplets.

Simulations with $1 < \text{We}_b < 20$ ($R_f^* = 5$ and 10) show a behaviour similar to the one depicted in Fig. 3: The large droplets result from interstitial liquid and are initially inter-connected by ligaments. Secondary satellite droplets form when these ligaments are pinched at both ends and break. The result is a spray with a bidisperse droplet distribution. For cases with $\text{We}_b \approx 1$, pinching occurs in the centre of the ligament and smaller or even no satellite droplets are formed. This behaviour is comparable to droplet collisions at high Weber numbers [14], although each droplet is simultaneously connected to more than one neighbour in the present context. The diameter of the main interstitial droplets is roughly equal $2R_f$ as can be geometrically predicted for this kind of regular arrangement. Outside of the $1 < \text{We}_b < 20$ range, distinctly different break-up scenarios are observed as shown in Fig 5. For $\text{We}_b < 1$ groups of droplets detach from the bulk of the liquid while still being connected through thick ligaments. Since surface tension forces are larger than the momentum of the droplets, the groups coalesce into droplets that are larger than the initial interstitial volumes, and this is shown in Fig. 5(a). In cases with $\text{We}_b > 20$, see Figs. 5(b) and (c), the bubbles have a larger deformation prior to coalescence, leading to the formation of liquid lamellae where the two interfaces are aligned and approximately parallel to each other. Further stretching and evaporation lead to extremely thin lamellae that eventually burst (Fig. 5(b)). The bursting effect and the resulting droplet size are affected by the grid resolution. It occurs when the grid resolution is no longer adequate to calculate the surface tension using the CSS model [22]. However, this is also partially caused by the highly regular bubble distribution used here and more natural break-up patterns are expected for more randomly deformed lamellae as observed e.g. in bag-like break-up of droplets [15]. In some cases, the artificial droplets are sufficiently small and quickly evaporate, allowing to observe the break-up of the lamella rims that can be associated with the remaining inter-connected interstitial liquid (see Fig. 5(c)). There, the connecting ligaments break in irregular patterns. This yields a rather mono-disperse spray of droplets that are much smaller than the final bubble size. The irregular break-up of the ligaments is comparable to aerodynamic break-up and correlates with a larger Reynolds number ($\text{Re}_b > 100$). Both the artificial lamella bursting and the ligament break-up patterns indicate that finer mesh resolutions are required for these cases to prevent premature bursting and to ensure the resolution the Kolmogorov scale associated with the aerodynamic break-up.

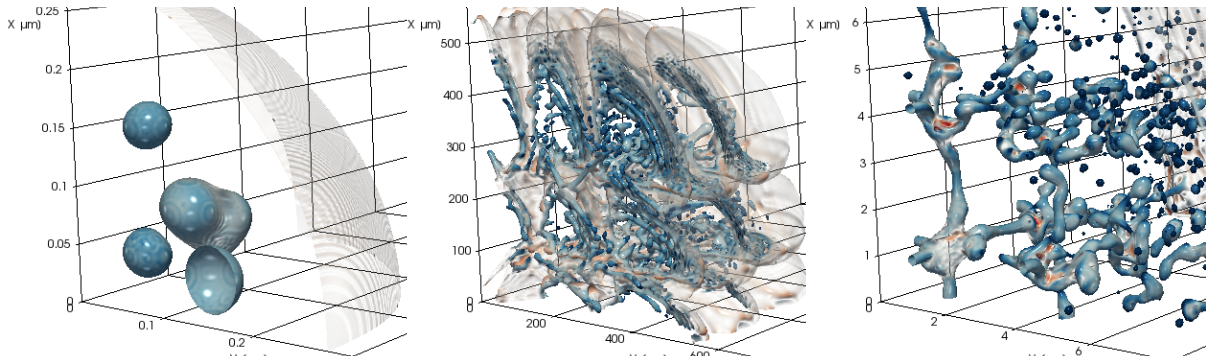

(a) $\text{We}_b < 1$ Coalescing droplets (b) $\text{We}_b > 20$ Artificial Lamella bursting (c) $\text{We}_b > 20$ Irregular ligament break-up

Figure 5. Alternative break-up behaviours found in different test cases

It is noted here that the size of the small droplets resulting from ligament pinching and lamella bursting can be affected by the mesh size and further grid refinement studies are to be conducted. The larger droplet size distribution can be affected by the initial bubble locations (regular vs. irregular arrays). However, the qualitative characterization of the break-up process is likely to be unaffected as it is largely determined by We_b and Oh_b.

Conclusions

In this work, a framework is established to simulate the primary break-up processes in a jet undergoing flash atomization. The conditions are representative of the injection of liquid oxygen in the low pressure combustion chamber of a rocket thruster in space. The liquid injection temperature and the chamber pressure are the primary parameters characterizing the flashing behaviour of a jet. Additionally, the merging bubble radius is used as a free parameter which could be related to nucleation rates.

We use a multiphase DNS solver, where fluid properties and evaporation mass fluxes are obtained from pre-

computed one-dimensional solutions for the growth of isolated bubbles. This approach implies a uniform bubble distribution, but this assumption can be relaxed in future work by coupling the evaporation rates with the solution of the energy equation.

It is shown that the droplet formation process and resulting spray characteristics can be correlated through characteristic quantities, and distinct break-up processes dependent on these quantities can be identified. For intermediate Weber numbers, stretching of cylindrical ligaments leads to a bidisperse droplet distribution of the spray. For cases with a high bubble density and low Weber numbers, droplet coalescence is more likely to occur. For larger Weber numbers, however, the merging of bubbles at large radii leads to the formation of thin lamellae and aerodynamic break-up. Here, some uncertainties in the quantitative analysis of the resulting droplet distribution remain and further studies with respect to the influence of mesh resolution on final droplet size are required.

Considering the relatively low computational cost, the method presented here shows potential for accurately capturing all the relevant physical processes in a flash atomization process. Future work will rely on the use of high performance computing to improve mesh resolution as well as bubble number and domain size such that truly predictive computational experiments can be performed.

Acknowledgements

This work is part of the HAoS-ITN project and has received funding from the European Union's Horizon 2020 research and innovation programme under the Marie Skłodowska-Curie grant agreement No 675676 (DL). We also acknowledge funding by DFG through the Collaborative Research Center SFB-TRR75 (DD, JR, AK, BW) and by the UK's Engineering and Physical Science Research Council support through the grant EP/P012744/1 (KV).

References

[1] Hurlbert, E., et al., 1998. *Journal of Propulsion and Power, 14*(5), p. 676–687.
[2] Manfletti, C., 2014. *Journal of Propulsion and Power, 30*(4), pp. 925–933.
[3] Blander, M., and Katz, J. L., 1975. *AIChE Journal, 21*(5), pp. 833–848.
[4] Lamanna, G., et al., 2014. *International Journal of Multiphase Flow, 58*, pp. 168 – 184.
[5] Lamanna, G., et al., 2015. *Atomization and Sprays, 25*(10), pp. 837–856.
[6] Luo, M., and Haidn, O. J., 2016. *Journal of Propulsion and Power, 32*(5), p. 1253–1263.
[7] Price, C., et al., 2016. *Atomization and Sprays, 26*(12), pp. 1197–1239.
[8] Karathanassis, I., et al., 2017. *International Journal of Multiphase Flow, 95*, pp. 257–270.
[9] Saha, K., et al., 2016. *Journal of Energy Resources Technology, 138*(5), p. 052208.
[10] Calay, R., and Holdo, A., 2008. *Journal of Hazardous Materials, 154*(1-3), pp. 1198–1209.
[11] Schmehl, R., and Steelant, J., 2009. *Journal of Propulsion and Power, 25*(3), pp. 771–782.
[12] Zeng, Y., and Lee, C.-F. F., 2001. *Combustion Science and Technology, 169*(1), pp. 45–67.
[13] Rayleigh, Lord, 1878. *Proceedings of the London mathematical society, 1*(1), pp. 4–13.
[14] Roisman, I. V., 2004. *Physics of Fluids, 16*(9), pp. 3438–3449.
[15] Opfer, L., et al., 2012. In 12th International Conference on Liquid Atomization and Spray Systems (ICLASS), Heidelberg, Germany.
[16] Lee, H. S., and Merte, H., 1996. *International Journal of Heat and Mass Transfer, 39*(12), pp. 2427–2447.
[17] Bell, I. H., et al., 2014. In *Industrial & Engineering Chemistry Research*, Vol. 53. pp. 2498–2508.
[18] Eisenschmidt, K., et al., 2016. *Journal of Applied Mathematics and Computation, 272*(2), 1, pp. 508–517.
[19] Lafaurie, B., et al., 1994. *Journal of Computational Physics, 113*(1), pp. 134 – 147.
[20] Schlottke, J., and Weigand, B., 2008. *Journal of Computational Physics, 227*(10), May, p. 5215–5237.
[21] Thompson, A. S., and Heister, S. D., 2016. *Atomization and Sprays, 26*(7), p. 633–658.
[22] Liu, M., and Bothe, D., 2016. *Journal of Fluid Mechanics, 789*, 02, pp. 785–805.